nature geoscience

ARTICLES

https://doi.org/10.1038/s41561-020-0553-x

Check for updates

Larger tsunamis from megathrust earthquakes where slab dip is reduced

Bar Oryan ✉ and W. Roger Buck

A subset of megathrust earthquakes produce anomalously large tsunamis for their magnitude. All of these recorded 'tsunami earthquakes' in the past 50 years had extensional aftershocks in the upper plate. These include the two largest and most destructive earthquakes of that period, the 2004 Sumatra–Andaman and the 2011 Tohoku events. Evidence from the region of Tohoku indicates that normal fault slip in the upper plate during the earthquake may have contributed to the tsunami size. Here we present a numerical model that shows how a reduction of the dip of a subducting slab, on a timescale of millions of years, can result in an extensional fault failure above a megathrust earthquake on timescales of seconds to months. Slab dip reduction bends the upper plate so that the shallow part fails in extension when a megathrust rupture relieves compressional stress. This results in a distribution of extensional aftershocks comparable to that seen above the Tohoku megathrust. Volcanic arc migration and uplift data for Tohoku and several other tsunami earthquakes is consistent with slab dip reduction. The collection of more such data might identify other areas of tsunami hazard related to slab dip reduction.

The unparalleled data collected before, during and after the M_w 9.1 Tohoku tsunami earthquake off the Pacific coast of Japan[1] defied conventional wisdom in a number of ways. Seafloor displacement measurements for this earthquake are constrained by multibeam bathymetric surveys[2,3], cabled ocean-bottom tsunami sensors[4] and land-based and seafloor geodesy[5,6], and suggest that maximum displacements of ~60 m occurred close to the ocean floor at the trench[1,7–10]. This 'slip to the trench' behaviour was not expected, as it is believed that the shallow portion of the subduction interface is frictionally stable so that little stress would accumulate over the period between great earthquakes[11–13]. Typically, the greatest amount of displacement for megathrust earthquakes is concentrated between depths of ~15 and ~35 km[14].

The propagation of the Tohoku megathrust rupture all the way to the surface contributed significantly to a tsunami[4] that resulted in a large number of fatalities and the costliest natural disaster in history[15]. Based on seafloor mapping and geodesy[2,3,5], this shallow megathrust slip appears to be related to coseismic slip on a major normal fault with a breakaway about 50 km west of the Japan Trench, where fresh fault scarps and hydrothermal activity were observed after the main earthquake[16]. Multichannel seismic data indicate that this normal fault has been active for millions of years[17].

Postseismic extension of the plate above the Tohoku megathrust produced a wide region of normal faulting earthquakes. For about 6 months after the Tohoku mainshock, nearly 2,000 aftershocks were recorded, most of which were extensional and located in the upper plate, up to 230 km west of the trench and to a depth of ~30 km (refs [18,19]) (Fig. 1). Moreover, borehole stress measurements[20] and stress tensor inversion of the foreshocks[18] suggest that preceding the megathrust event the maximum compressive stress (σ_1) was oriented in the direction of plate convergence. After the megathrust, the minimum compressive stress (σ_3) was pointing in the direction of plate convergence[18]. Such a radical change in the stress field after a megathrust event had not been seen before and, combined with the observation of slip to the trench, suggests a nearly total stress drop on the megathrust during a great earthquake[21,22].

The 2004 M_w 9.2 Sumatra–Andaman earthquake[23,24], the strongest earthquake in the past 50 years, ruptured over a 1,300 km long section of the Sunda subduction system, and reached displacements of up to 20 m. As for the Tohoku, event this earthquake produced extensional aftershocks in the plate above the subduction interface as well as an extremely large tsunami, which made it a 'tsunami earthquake'[25].

A 'tsunamigenic earthquake' is any earthquake that produces a tsunami. In contrast, a tsunami earthquake produces a larger than expected tsunami for its surface wave magnitude[26]. Most megathrust earthquakes are not associated with extensional upper plate aftershocks. However, all tsunami earthquakes since the 1970s had extensional aftershocks in the upper plate[25,27] (Fig. 2). Seismic data from earlier tsunami earthquakes may lack the required resolution to accurately locate and define the mechanism of upper plate aftershocks.

The upper plate extension in areas of plate convergence is surprising, and the association between normal faulting and tsunami size has led to discussion into the ways that such deformations caused. Two ideas for upper plate extension are based on the concept of a total stress drop on the subduction interface. Several authors suggest that complete weakening of the megathrust may produce an inertial 'overshoot' of the upper plate that puts it in extension[21,28]. However, an overshoot of 60 m could produce an average strain of $\sim 3 \times 10^{-4}$ over a 200 km wide region to produce roughly 10 MPa of extensional stress (Supplementary Table 4). Given the lithostatic stresses prior to the earthquake, this would be enough to drive normal fault slip to about 1 km in depth (assuming normal friction and zero cohesion[29]), rather than to the >20 km depths observed. The alternative idea that gravitational potential energy drives normal faulting[25] requires nearly zero strength on those normal faults[30,31].

Upper plate extension due to slab dip reduction

Here we consider how bending may drive slip on strong normal faults in the upper plate of a subduction system. Bending is the accepted way to explain the frequently observed extensional earthquakes and surface-cutting normal faults seen for the lower plates

Lamont-Doherty Earth Observatory, Earth Institute at Columbia University, Palisades, NY, USA. ✉e-mail: boryan@ldeo.columbia.edu

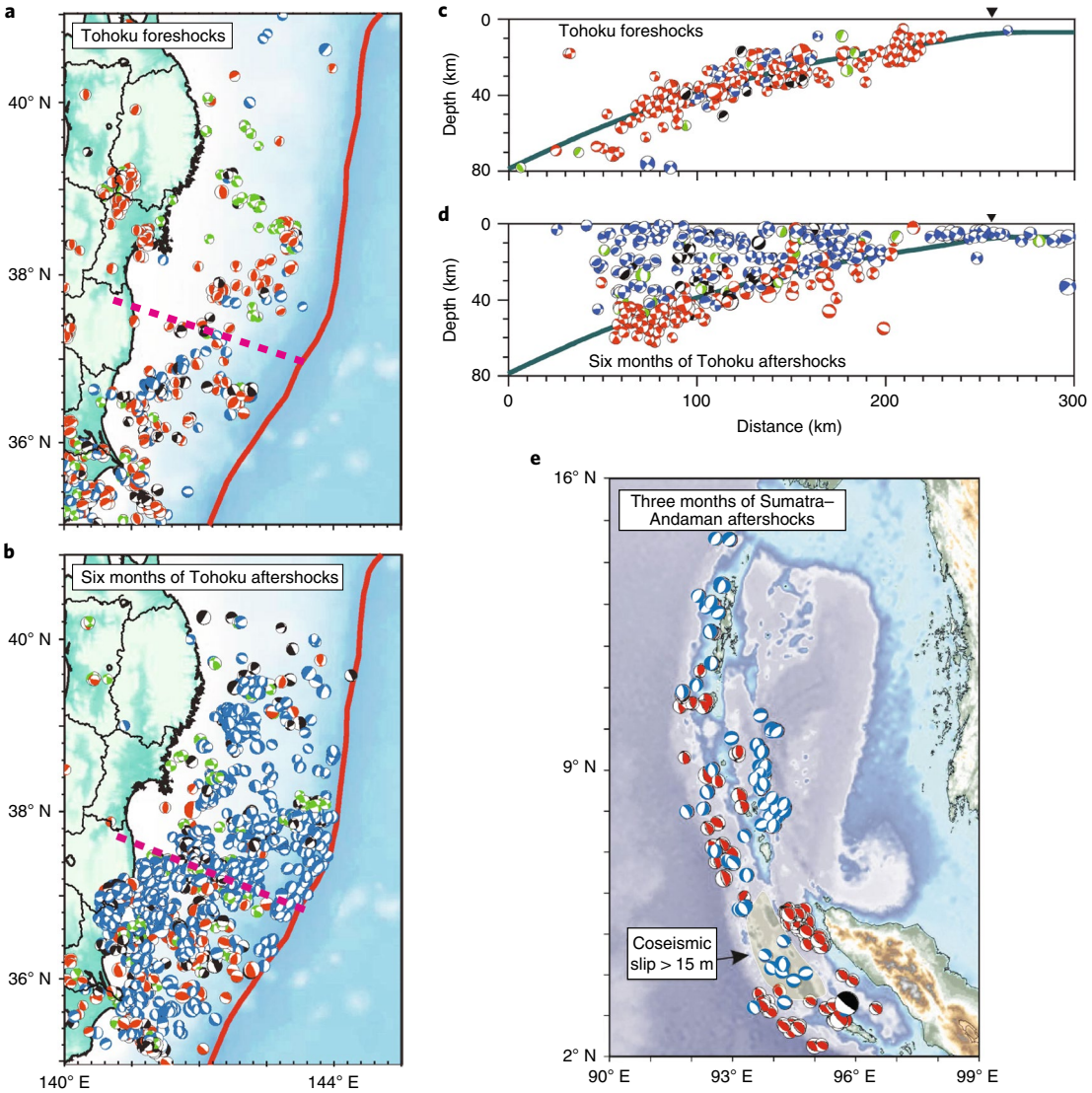

Fig. 1 | Foreshocks and aftershocks for the Tohoku and Sumatra–Andaman megathrust earthquakes. Beach balls represent extensional (blue), strike-slip (green), compressive (red) and other types of focal mechanism (black) earthquakes. **a**, Upper plate Tohoku foreshocks. **b**, Upper plate Tohoku aftershocks over six months. The solid red line marks the Japan Trench. The red dashed line denotes the location of the profile shown in **c** and **d**. **c**,**d**, Profiles of the distribution of the upper plate Tohoku foreshocks (**c**) and six months of aftershocks (**d**) with depth. Black triangles indicate the location of the trench. **e**, Three months of aftershocks following the Sumatra–Andaman event (marked by a large black beach ball). Panels **a**–**d** adapted with permission from ref. [18], Elsevier, and panel **e** with permission from ref. [25], Elsevier.

of subduction systems[32]. The lower plate bends as it plunges into the Earth's interior. However, the cause of upper plate bending and extension is not obvious.

Reduction in the dip of a subducting slab should gradually bend the upper plate so that its top yields in extension[19,33,34]. We postulate that extensional aftershocks can result from the interaction of stresses produced by such bending on a geological timescale with stresses that vary through an earthquake cycle (Fig. 3). During an interseismic period, when the fault is locked, build-up of shear stress along the subduction interface results in horizontal compression through the upper plate. Continued plate bending during the interseismic period adds extensional stress at a slower rate than the compressional stress build-up due to convergence. Dynamic weakening of the subduction interface during a major earthquake relieves shear-related compressional stresses[35]. This allows upper plate normal fault slip that releases the elastic bending stresses that accumulated during the interseismic period.

Long-term stress changes due to upper plate bending

To test this concept, we simulated both the long-term evolution of a subduction system and the short-term release of stresses during and after an earthquake. We used the Fast Lagrangian Analysis of Continua (FLAC) solution for momentum conservation[36]. This code is capable of simulating elastic, viscous and plastic deformation, all of which are pertinent to our conceptual model. FLAC has been used to model the long-term development of subduction zones[37], as well as in models that include long-term and short-term processes that affect earthquake cycles[38]. As in other models of earthquake cycles on subduction zones[39], we used time steps on the order of years to simulate subduction evolution and time steps on the order of seconds for coseismic deformation. The Methods section describes our numerical approach in detail.

Gradual changes in the slab dip angle are induced by changing the velocity of the asthenosphere relative to that of the upper plate. We considered three different histories of dip change. The top row

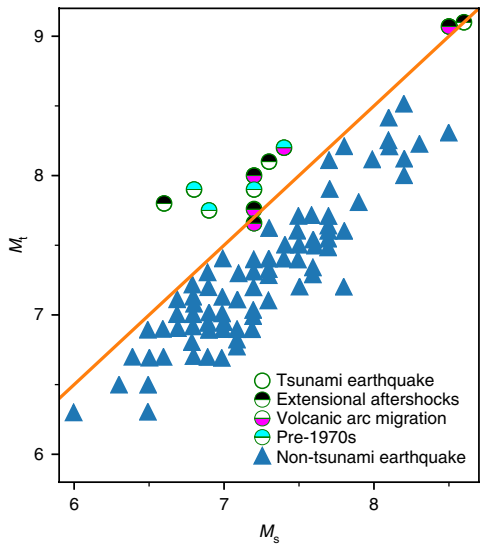

Fig. 2 | Plot of tsunami magnitude (M_t) versus surface wave moment (M_s) for earthquakes that generated tsunamis. The triangles indicate earthquakes in the region of Japan that generated tsunamis but did not meet the definition of a tsunami earthquake (data from ref. [48]). Circles are earthquakes that meet the seismic spectral definition of tsunami earthquakes[14,26]. Tsunami earthquakes with extensional upper plate aftershocks or insufficient seismological data to identify the upper plate aftershocks are denoted by a black or cyan fill, respectively. A magenta fill denotes earthquakes that are consistent with the migration of the associated volcanic arc, which indicates a slab dip decrease. The orange line denotes the linear relation of $M_t = M_s + 0.5$ (see Methods, Supplementary Table 1 and Supplementary Section 1). Values are unitless numbers.

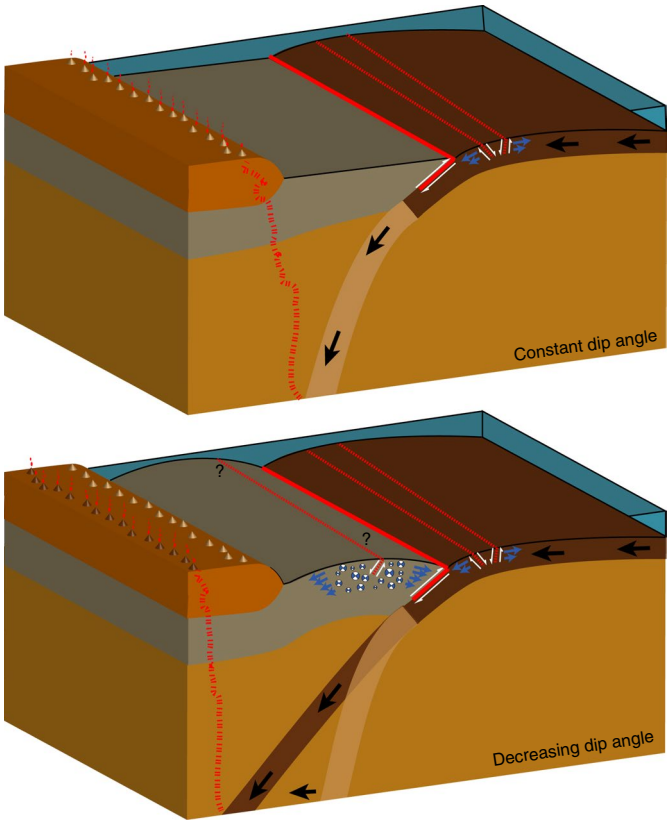

Fig. 3 | Cartoon showing the effect of decreasing the subducting slab dip angle on upper plate bending, and the location of the volcanic arc. Blue beach balls indicate extensional aftershocks after a megathrust rupture on the interface, indicated in red. Blue arrows signify extensional bending stresses. The red dashed lines denote the location of normal faults. Question marks denote the possible location of a normal fault in the upper plate. White arrows indicate the direction of fault slip. Cones represent the location of volcanic arcs (red dashes on the left show the active arc).

of Fig. 4 shows the thermal and stress fields after 260 km of convergence when the deeper mantle (asthenosphere) was fixed relative to the upper plate (constant dip angle case). For the other two cases shown in Fig. 4, 100 km of convergence was accumulated before the velocity of the asthenosphere was altered. To impose a decrease (increase) in the dip angle we forced the asthenosphere to migrate in the same (opposite) horizontal direction as the downgoing plate (Fig. 4). The middle row shows the results after a 3° increase in the slab dip angle and the bottom row shows results for a similar decrease in slab dip.

The results show that the upper plate stress state depends strongly on whether and how the slab dip changed. In the case of a progressive increase in slab dip (middle row in Fig. 4), the top of the upper plate is put into compression as the upper plate is bent in a concave-up sense. In contrast, a progressive decrease in slab dip (lower row in Fig. 4) leads to a broad and deep region of extensional stresses due to bending rather than other reasons[40] (Supplementary Section 2). These stresses are sufficient to cause brittle yielding of a broad shallow region of the upper plate. Moreover, dip decrease (increase) results in far-field compression (extension).

The topography of the upper plate was strongly affected by the imposed boundary conditions related to slab dip changes. The increase in slab dip shown in the middle row of Fig. 4 led to subsidence of a few kilometres in the central part of the plate above the subduction interface. The slab dip decrease indicated in the bottom row of Fig. 4 produced a similar magnitude of uplift of that region.

Short-term stress changes to the upper plate after a megathrust event

To illustrate the stress changes during an earthquake cycle for the dip decrease case we considered changes in Coulomb stresses[41], a measure of how close a fault is to frictional slip. The Coulomb stress is defined as the shear stress on a fault minus the shear stress needed for Coulomb failure (Methods). Figure 5a shows the Coulomb stress for ideally oriented fault planes (that is, with the largest values of Coulomb stress) at the end of a geologically long period when the subduction interface was taken to have zero strength. The dark blue zone in that figure, where the Coulomb stress is zero, is at the point of failure, or yield, in extension. Convergence for 1,000 years at a rate of 10 cm yr^{-1} and with the megathrust locked pushes the extensionally yielding area of the upper plate away from failure, as shown by the change in Coulomb stress shown in Fig. 5b. The release of compressional stress when the megathrust is unlocked causes a large region of the upper plate to fail in extension (Fig. 5c,d). An 'aftershock' was plotted for each element that reached extensional failure and accumulated plastic strain for multiple time steps. For cases without reduction in slab dip, the numerical models did not predict extensional earthquakes in the upper plate during an earthquake cycle, as shown in the Supplementary Information.

The model includes both inertial and gravitational stress changes and complete weakening of the megathrust during a model earthquake. Thus, our results cast doubt on the idea that a complete megathrust stress drop alone (that is, without dip reduction) produces extensional aftershocks due to either stress rotation[21,22] or inertial overshoot[28] unless the upper plate faults are extremely weak.

Our results demonstrate that a reduction in the dip of a subducting slab can produce an extensional stress state in the upper plate of

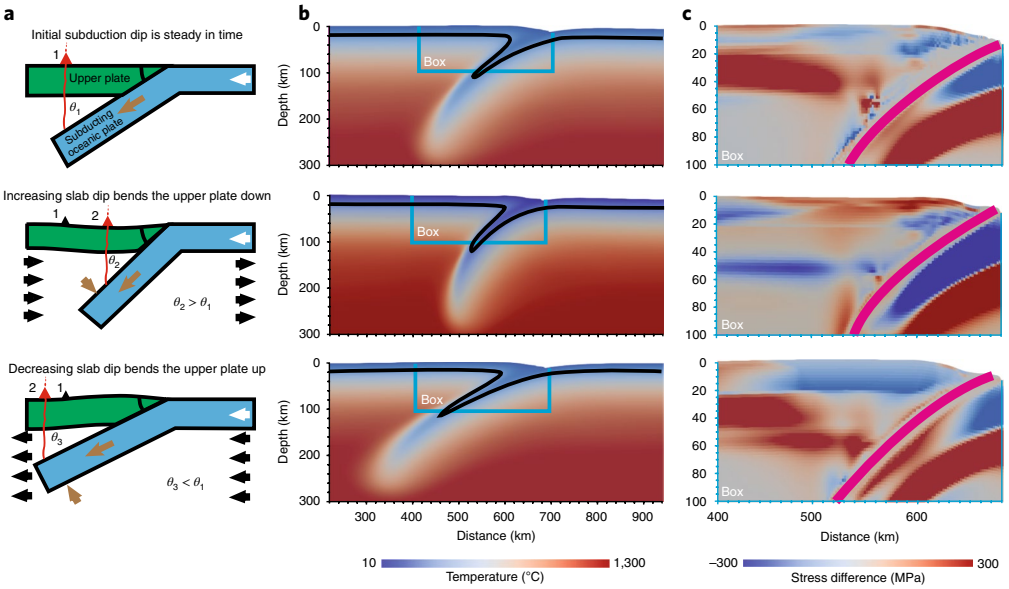

Fig. 4 | Snapshots showing how slab dip changes can alter the upper plate stress state. The top row is for a relatively constant dip angle, the middle row for about a 3° increase in the slab dip angle and the bottom row shows an about 3° decrease in the slab dip angle. **a**, The conceptual model that links slab dip changes to bending of the upper plate and to the position of the volcanic arc (red arrow shows the active arc). Black and white arrows denote the boundary conditions used to induce the dip angle changes and subduction convergence, respectively. Brown arrows denote the resulting movement of the plates. **b**, Temperature in the numerical model. Black lines denote the 250 °C contour. The cyan box represents the area of the stress difference (horizontal minus vertical) cross-sections in **c**. Magenta denotes the subduction interface with plastic strains higher than 1.

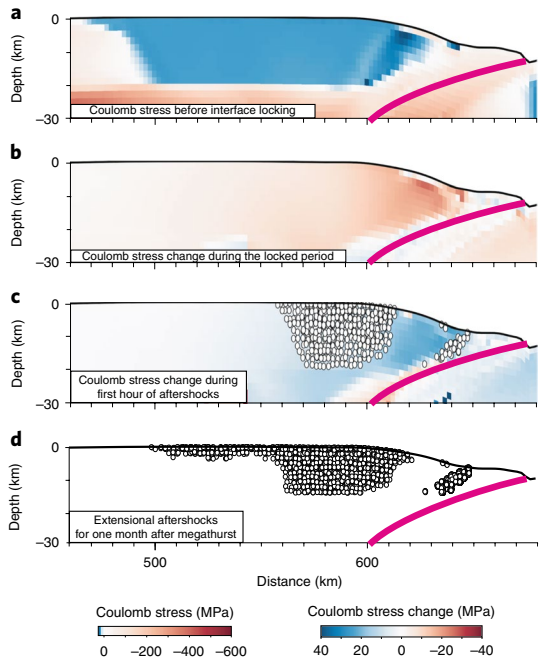

Fig. 5 | Illustration of stress changes through an earthquake cycle for the slab dip reduction case. a, Full Coulomb stresses on ideally oriented fault planes just before the interface is locked (zero indicates fault at failure). Coulomb stress is the shear stress on a fault minus the shear stress needed for brittle failure. **b**, Coulomb stress change from the beginning to the end of the 1,000 yr locked period. **c**, Coulomb stress change from the end of the locked period to an hour after the megathrust event. White circles indicate extensional aftershocks. **d**, Extensional aftershocks within 30 days of the megathrust event. Magenta denotes the subduction interface with plastic strains higher than 1. The animation in Supplementary Video 1 illustrates the Coulomb stress change and extensional aftershocks with time.

a subduction system. Furthermore, we show that locking of a subduction interface during the interval between great earthquakes can suppress the extensional brittle yielding of the upper plate. Dynamic weakening along the entire megathrust can then lead to extensional aftershocks over a broad region of the upper plate. For a case in which the upper plate has a lithospheric thickness of ~70 km, the model generated extensional aftershocks over a region 160 km wide and 20 km deep, dimensions comparable to those observed after the Tohoku earthquake.

Comparing model results to geological observations

Two lines of evidence suggest an ongoing reduction of the dip of the slab descending at the Japan Trench: arc migration and long-term uplift of the upper plate. The strongest evidence derives from dating past positions of the volcanic arc on Honshu. The position of the arc is thought to reflect the depth at which water is liberated from the downgoing slab that produces a partial melt in the hot mantle wedge that rises vertically to build a volcanic arc[42]. Migration of the arc away from the trench would then indicate a reduction of the slab dip. Geological data demonstrate that the volcanic arc moved trenchwards through the mid-Miocene and that it started migrating away from trench sometime in the past 20 Myr[43] (Fig. 6a).

Further support for the change in slab dip angle comes from boreholes drilled in the upper plate west of the Japan Trench[44]. Upper plate subsidence curves constrained by foraminifera assemblages and corrected for sediment compaction and loading were calculated for Deep Sea Drilling Project sites 438/439 at about 110 km from the present-day trench[44] (Fig. 6b). These curves show subsidence from about 25 million years ago (Ma) to about 4 Ma followed by uplift for sites 438/439. These sites are north of the Tohoku rupture area, but they constitute the best constraints available on long-term upper plate subsidence and uplift trends.

We simulated a period of rapid slab dip increase followed by a period of dip reduction. We used the same ratio of subsidence to uplift duration as was observed at sites 438/439. The modelled upper plate subsidence trend and changes in dip angle are consistent

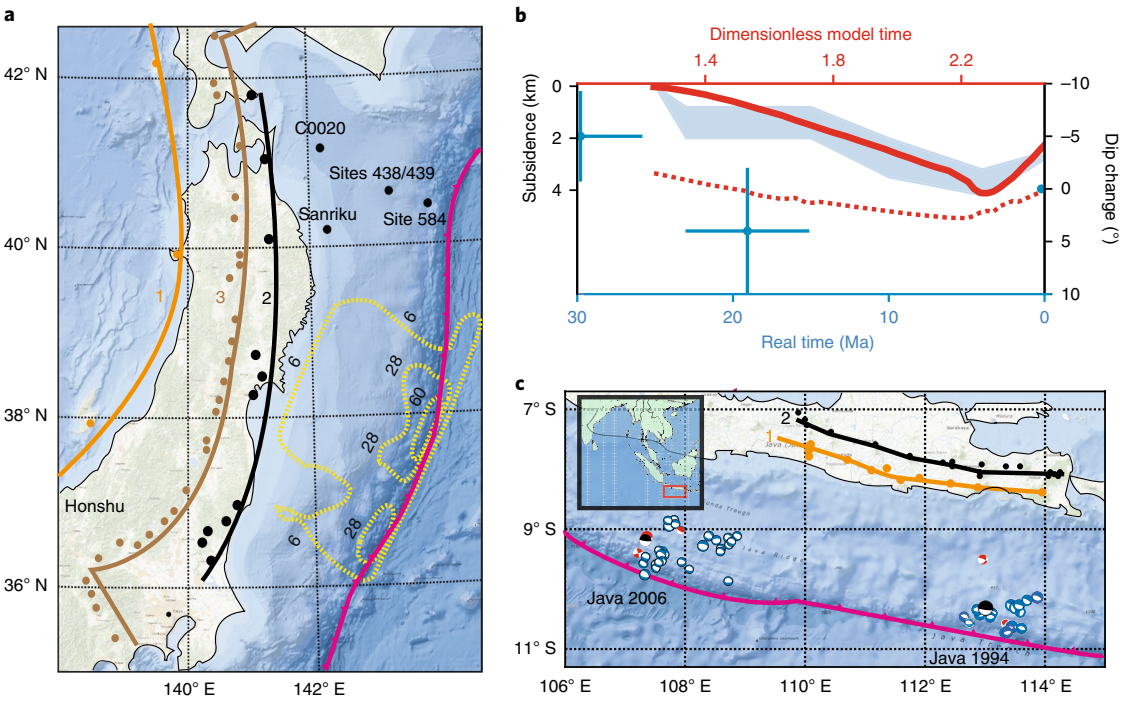

Fig. 6 | Evidence of slab dip reduction over time at the Japan and Java Trenches where tsunami earthquakes have occurred. a, Map showing the location of the volcanic arc on Honshu at three times, as indicated by coloured and numbered lines: ~30 Ma (1, orange), ~20 Ma (2, black) and present (3, brown)[43]. Dots indicate arc volcanoes. The locations of drill sites used to constrain subsidence and uplift are shown in black. The magenta line denotes the location of the trench. The dashed yellow contours denote the inferred slip in metres for the Tohoku Earthquake[49]. **b**, The blue shading denotes the possible subsidence solutions for sites 438/439 at a distance of 110 km from the trench[44]. The solid red curve denotes the subsidence computed by our model at the same position. Blue dots with error bars show the estimated change in slab dip relative to the present dip based on the position of volcanic arc[43] (see Methods). The dashed red line shows the change of the dip angle of the numerical model. **c**, Map showing the locations of the Java 1994 and 2006 tsunami earthquakes (black beachballs) and roughly 4 months of extensional and compressional aftershocks as indicated by blue and red beachballs, respectively. The locations of the volcanic arc in Java at two different times are indicated by coloured and numbered lines, ~20 Ma (1, orange) and present (2, black)[50]. Inset: The red box shows the location of the main map. Panel **c** adapted with permission from ref. [25], Elsevier.

with those observed (Fig. 6b). There is a particularly good correlation between the uplift observed at sites 438/439 since ~4 Ma and the uplift generated by the numerical model. Sites C0020, 584 and Sanriku show subsidence for the period in which uplift occurred for sites 438/439[44]. Our numerical model captured this behaviour as it shows the maximum uplift at a distance of about 150 km from the trench along with subsidence closer and further away from the trench (Supplementary Fig. 3). Upper plate stresses far from the trench (600 km away in the model) are also consistent with observations. During the period of slab dip increase the model far-field stresses are extensional and consistent with the opening of the Sea of Japan. During the slab dip decrease these stresses are compressional (Supplementary Fig. 1), which agrees with the transition to thrusting across much of Honshu and into the Sea of Japan[44]. This model sequence also produces normal aftershocks in a region comparable in dimension to those observed following the Tohoku earthquake.

Extensional faulting in a region of plate convergence has added fuel to the debate over the strength of faults. These faults are suggested to be so weak that they can slip at stresses as small as a few MPa[18,21,45]. This conflicts with observations from lab measurements of fault properties and stresses in boreholes from around the globe, which indicate most faults are far stronger[46]. Our model predicts that the upper plate above the Japan megathrust is strong and subject to large (>150 MPa for the deeper aftershocks) extensional stress differences. Testing this requires drilling to a depth of at least 2 km.

As was shown before, slab dip reduction produces both bending and uplift that act to produce extensional stresses in the upper plate above a subduction interface. Some of the largest modelled extensional stresses occur in a similar location, relative to the trench, as the major normal fault that was active during the Tohoku earthquake and that may have contributed to the tsunami size[16,17]. Although our present model does not consider an existing normal fault in that location, it suggests why such a fault might slip if a megathrust event causes dynamic weakening of the interface. Such interface weakening has been called on to allow gravitational stresses to produce slip on such a normal fault, as long as that fault is very weak[25]. The present model suggests how normal faults that are too strong to fail due to gravitational stresses alone could be activated at subduction zones with a history of decreasing slab dips, which increases the tsunami risk.

To further validate our model, we examined all the published data on arc migration and upper plate uplift for regions in which extensional aftershocks were observed following tsunami earthquakes. The direction of arc migration is only documented for three regions: Nicaragua (1992)[47], Java (1994 and 2006; Fig. 6c) and Japan (1896 and 2011; Fig. 6a). For these cases arc locations are consistent with slab dip reduction. The only available long-term uplift data for the region of extensional aftershocks associated with a tsunami earthquake are the data discussed above for the Japan trench. Data regarding uplift on the timescale of millions of years are hard to obtain as this requires drilling in the upper plate. Collecting such datasets in other regions has the potential to better estimate the tsunami hazard.

Online content

Any methods, additional references, Nature Research reporting summaries, source data, extended data, supplementary information, acknowledgements, peer review information; details of author contributions and competing interests; and statements of data and code availability are available at https://doi.org/10.1038/s41561-020-0553-x.

Received: 24 December 2018; Accepted: 11 February 2020;
Published online: 16 March 2020

References

1. Lay, T. A review of the rupture characteristics of the 2011 Tohoku-oki M_w 9.1 earthquake. *Tectonophysics* **733**, 4–36 (2018).
2. Fujiwara, T. et al. The 2011 Tohoku-Oki earthquake: displacement reaching the trench axis. *Science* **334**, 1240 (2011).
3. Sun, T., Wang, K., Fujiwara, T., Kodaira, S. & He, J. Large fault slip peaking at trench in the 2011 Tohoku-oki earthquake. *Nat. Commun,* **8**, 14044 (2017).
4. Maeda, T., Furumura, T., Sakai, S. & Shinohara, M. Significant tsunami observed at ocean-bottom pressure gauges during the 2011 off the Pacific coast of Tohoku Earthquake. *Earth Planets Space* **63**, 803–808 (2011).
5. Sato, M. et al. Displacement above the hypocenter of the 2011 Tohoku-Oki earthquake. *Science* **332**, 1395 (2011).
6. Iinuma, T. et al. Coseismic slip distribution of the 2011 off the Pacific Coast of Tohoku earthquake (M9.0) refined by means of seafloor geodetic data. *J. Geophys. Res. Solid Earth* **117**, B07409 (2012).
7. Simons, M. et al. The 2011 magnitude 9.0 Tohoku-Oki earthquake: mosaicking the megathrust from seconds to centuries. *Science* **332**, 1421–1425 (2011).
8. Fujii, Y., Satake, K., Sakai, S., Shinohara, M. & Kanazawa, T. Tsunami source of the 2011 off the Pacific coast of Tohoku earthquake. *Earth Planets Space* **63**, 815–820 (2011).
9. Yagi, Y. & Fukahata, Y. Rupture process of the 2011 Tohoku-oki earthquake and absolute elastic strain release. *Geophys. Res. Lett.* **38**, L19307 (2011).
10. Shao, G., Li, X., Ji, C. & Maeda, T. Focal mechanism and slip history of the 2011 M_w 9.1 off the Pacific coast of Tohoku earthquake, constrained with teleseismic body and surface waves. *Earth Planets Space* **63**, 559–564 (2011).
11. Hyndman, R. D., Yamano, M. & Oleskevich, D. A. The seismogenic zone of subduction thrust faults. *Isl. Arc* **6**, 244–260 (1997).
12. Byrne, D. E., Davis, D. M. & Sykes, L. R. Loci and maximum size of thrust earthquakes and the mechanics of the shallow region of subduction zones. *Tectonics* **7**, 833–857 (1988).
13. Moore, J. C. & Saffer, D. Updip limit of the seismogenic zone beneath the accretionary prism of Southwest Japan: an effect of diagenetic to low-grade metamorphic processes and increasing effective stress. *Geology* **29**, 183–186 (2001).
14. Lay, T. et al. Depth-varying rupture properties of subduction zone megathrust faults. *J. Geophys. Res. Solid Earth* **117**, B04311 (2012).
15. Kajitani, Y., Chang, S. E. & Tatano, H. Economic impacts of the 2011 Tohoku-oki earthquake and tsunami. *Earthq. Spectra* **39**, 457–478 (2013).
16. Tsuji, T. et al. Extension of continental crust by anelastic deformation during the 2011 Tohoku-oki earthquake: the role of extensional faulting in the generation of a great tsunami. *Earth Planet. Sci. Lett.* **364**, 44–58 (2013).
17. Tsuji, T. et al. Potential tsunamigenic faults of the 2011 off the Pacific coast of Tohoku Earthquake. *Earth Planets Space* **63**, 58 (2011).
18. Hasegawa, A. et al. Change in stress field after the 2011 great Tohoku-Oki earthquake. *Earth Planet. Sci. Lett.* **355–356**, 231–243 (2012).
19. Imanishi, K., Ando, R. & Kuwahara, Y. Unusual shallow normal-faulting earthquake sequence in compressional northeast Japan activated after the 2011 off the Pacific coast of Tohoku earthquake. *Geophys. Res. Lett.* **39**, L09306 (2012).
20. Lin, W. et al. Principal horizontal stress orientations prior to the 2011 M_w 9.0 Tohoku-Oki, Japan, earthquake in its source area. *Geophys. Res. Lett.* **38**, L00G10 (2011).
21. Hardebeck, J. L. Coseismic and postseismic stress rotations due to great subduction zone earthquakes. *Geophys. Res. Lett.* **39**, L21313 (2012).
22. Hasegawa, A., Yoshida, K. & Okada, T. Nearly complete stress drop in the 2011 M_w 9.0 off the Pacific coast of Tohoku Earthquake. *Earth Planets Space* **63**, 703–707 (2011).
23. Ishii, M., Shearer, P. M., Houston, H. & Vidale, J. E. Extent, duration and speed of the 2004 Sumatra–Andaman earthquake imaged by the Hi-Net array. *Nature* **435**, 933–936 (2005).
24. Ammon, C. J. et al. Rupture process of the 2004 Sumatra–Andaman earthquake. *Science* **308**, 1133–1139 (2005).
25. McKenzie, D. & Jackson, J. Tsunami earthquake generation by the release of gravitational potential energy. *Earth Planet. Sci. Lett.* **345–348**, 1–8 (2012).
26. Kanamori, H. Mechanism of tsunami earthquakes. *Phys. Earth Planet. Inter.* **6**, 346–359 (1972).
27. Polet, J. & Kanamori, H. Shallow subduction zone earthquakes and their tsunamigenic potential. *Geophys. J. Int.* **142**, 684–702 (2000).
28. Ide, S., Baltay, A. & Beroza, G. C. Shallow dynamic overshoot and energetic deep rupture in the 2011 M_w 9.0 Tohoku-Oki earthquake. *Science* **332**, 1426–1429 (2011).
29. Brace, W. F. & Kohlstedt, D. L. Limits on lithospheric stress imposed by laboratory experiments. *J. Geophys. Res. Solid Earth* **85**, 6248–6252 (1980).
30. Conin, M., Henry, P., Godard, V. & Bourlange, S. Splay fault slip in a subduction margin, a new model of evolution. *Earth Planet. Sci. Lett.* **341–344**, 170–175 (2012); erratum **357–358**, 423 (2012).
31. Cubas, N., Avouac, J. P., Souloumiac, P. & Leroy, Y. Megathrust friction determined from mechanical analysis of the forearc in the Maule earthquake area. *Earth Planet. Sci. Lett.* **381**, 92–103 (2013).
32. Christensen, D. H. & Ruff, L. J. Outer-rise earthquakes and seismic coupling. *Geophys. Res. Lett.* **10**, 697–700 (1983).
33. Buck, W. R., Lavier, L. L. & Petersen, K. D. in *AGU Fall Meeting Abstracts* T12C-01 (AGU, 2015).
34. Oryan, B. & Buck, W. R. in *AGU Fall Meeting Abstracts* T23F-0661 (AGU, 2017).
35. Sibson, R. H. Interactions between temperature and pore-fluid pressure during earthquake faulting and a mechanism for partial or total stress relief. *Nat. Phys. Sci.* **243**, 66–68 (1973).
36. Cundall, P. A. Numerical experiments on localization in frictional materials. *Ing. Arch.* **59**, 148–159 (1989).
37. Gurnis, M., Hall, C. & Lavier, L. Evolving force balance during incipient subduction. *Geochem. Geophys. Geosyst.* **5**, Q07001 (2004).
38. Biemiller, J. & Lavier, L. Earthquake supercycles as part of a spectrum of normal fault slip styles. *J. Geophys. Res. Solid Earth* **122**, 3221–3240 (2017).
39. Sobolev, S. V. & Muldashev, I. A. Modeling seismic cycles of great megathrust earthquakes across the scales with focus at postseismic phase. *Geochem. Geophys. Geosyst.* **18**, 4387–4408 (2017).
40. Lallemand, S., Heuret, A., Faccenna, C. & Funiciello, F. Subduction dynamics as revealed by trench migration. *Tectonics* **27**, TC3014 (2008).
41. King, G. C. P., Stein, R. S. & Lin, J. Static stress changes and the triggering of earthquakes. *Bull. Seismol. Soc. Am.* **84**, 935–953 (1994).
42. Tatsumi, Y., Hamilton, D. L. & Nesbitt, R. W. Chemical characteristics of fluid phase released from a subducted lithosphere and origin of arc magmas: evidence from high-pressure experiments and natural rocks. *J. Volcanol. Geotherm. Res.* **29**, 293–309 (1986).
43. Tatsumi, Y., Otofuji, Y.-I., Matsuda, T. & Nohda, S. Opening of the Sea of Japan back-arc basin by asthenospheric injection. *Tectonophysics* **166**, 317–329 (1989).
44. Regalla, C., Fisher, D. M., Kirby, E. & Furlong, K. P. Relationship between outer forearc subsidence and plate boundary kinematics along the Northeast Japan convergent margin. *Geochem. Geophys. Geosyst.* **14**, 5227–5243 (2013).
45. Wang, K. et al. Stable forearc stressed by a weak megathrust: mechanical and geodynamic implications of stress changes caused by the M = 9 Tohoku-Oki earthquake. *J. Geophys. Res. Solid Earth* **124**, 6179–6194 (2019).
46. Zoback, M. D., Townend, J. & Grollimund, B. Steady-state failure equilibrium and deformation of intraplate lithosphere. *Int. Geol. Rev.* **44**, 383–401 (2002).
47. Plank, T., Balzer, V. & Carr, M. Nicaraguan volcanoes record paleoceanographic changes accompanying closure of the Panama gateway. *Geology* **30**, 1087–1090 (2002).
48. Abe, K. Quantification of tsunamigenic earthquakes by the Mt scale. *Tectonophysics* **166**, 27–34 (1989).
49. Lay, T., Ammon, C. J., Kanamori, H., Xue, L. & Kim, M. J. Possible large near-trench slip during the 2011 M_w 9.0 off the Pacific coast of Tohoku earthquake. *Earth Planets Space* **63**, 687–692 (2011).
50. Smyth, H., Hall, R., Hamilton, J. & Kinny, P. East Java: Cenozoic basins, volcanoes and ancient basement. In *Proc. Indonesia Petroleum Association, 30th Annual Convention* 251–266 (Indonesian Petroleum Association, 2005).

Publisher's note Springer Nature remains neutral with regard to jurisdictional claims in published maps and institutional affiliations.

© The Author(s), under exclusive licence to Springer Nature Limited 2020

Methods

Compilation of seismic and tsunami data for different Tsunamigenic and Tsunami earthquakes. The data used to make Fig. 2 is based on two definitions of tsunami earthquakes. Tsunami earthquakes were first defined by Kanamori[26] who identified two relatively small earthquakes that produced extremely large tsunami heights. This definition and subsequent refinements of it concluded that a tsunami earthquake is one that radiated more seismic energy at low frequencies compared to those of normal earthquakes[14,27,51]. The earthquakes denoted by circles in Fig. 2 are those that meet the seismic definition of tsunami earthquake[14].

A tsunami earthquake can also be defined by correlating the magnitude of an earthquake to its resulting tsunami. Satakei and Tanioka[52] defined a tsunami earthquake as one that meets the criterion:

$$M_t > M_s + 0.5 \quad (1)$$

Tsunami magnitude was defined by Abe[48]:

$$M_t = \log D + \log A + 5.8 \quad (2)$$

where D is the maximum crest or trough amplitude of the tsunami waves in metres measured by tide gauges and A is the distance in kilometres from the earthquake epicentre to the tide station.

Numerical model set-up. To test how changes in the dip of a subducting slab could affect stresses through an earthquake cycle, we used a two-dimensional explicit numerical code that incorporated the FLAC solution for momentum conservation[36]. A detailed description of the method applied to long-term geodynamic problems can be found in the literature for previous models[53,54]. The advection and diffusion of heat used here are described by Lavier and Buck[55].

Many codes used for geodynamic models treat only viscous and brittle (or plastic) deformation. FLAC, however, includes elastic, viscous and plastic deformation. The inclusion of elasticity allows us to treat deformation on both geological timescales (on the order of millions of years) as well as coseismic timescales (on the order of seconds) in the same model. This is not the first time that FLAC has been used to investigate long-term stress build up with short-term processes that relieve stresses. Examples include magmatic dike intrusions[56] and earthquakes cycles[38].

FLAC has been also used to model long-term subduction evolution. To do that we followed the approach, geometry and boundary conditions used by Hall et al.[57] and Gurnis et al.[37]. A 1,200 km wide and 500 km deep domain with three different rheologies was used here. In the model, 8 km of 'oceanic' crust overlies the mantle on the right half of the domain and 25 km of 'continental' crust is assumed for the top of the left half of the domain (Supplementary Table 4). The initial temperature structure of the shallow 'lithosphere' is taken from a half-space cooling model for an oceanic plate 100 Myr old.

We treated viscoelastic plastic deformation with viscous flow described by a non-Newtonian temperature- and pressure-dependent flow law:

$$\dot{\varepsilon} = A\sigma^n \exp\left(\frac{E + PV}{RT}\right) \quad (3)$$

with strain rate $\dot{\varepsilon}$, preexponential factor A, stress σ, stress exponent n, gas constant R, activation energy E, pressure P, temperature T and activation volume V[58].

Brittle failure was computed assuming the Mohr Coulomb failure criteria:

$$\tau = f(\sigma_n - p) + C \quad (4)$$

where τ is the shear stress, f the friction coefficient, σ_n the normal stress, p the pore pressure and C the cohesion[59]. The cases described in the main text are for models with the hydrostatic pore pressure simulated by lowering the friction coefficient, as indicated in Supplementary Table 4.

The friction coefficient and cohesion were defined to linearly decrease with increasing plastic strain, ϵ_p, as has been done in many previous models of faulting in which faults are approximated by zones of strain localization[60]. The friction coefficient for an element is a function of the plastic strain there:

$$f(\epsilon_p) = f_1 + (f_2 - f_1)(\epsilon_p/\Delta\epsilon) \quad (5)$$

where f_1 is the reference value at zero plastic strain and f_2 is the value for $\epsilon_p \geq \Delta\epsilon$ ($\Delta\epsilon$ is set to 1). Cohesion is assumed to follow the same relation with f replaced by C. Minimum possible values for f and C were set to zero. The viscous, elastic and plastic properties we used are listed in Supplementary Table 4.

As our code treats both viscous and elastic deformation, two criteria have to be checked to ensure numerical stability. (1) Time steps must be smaller than the Maxwell time for viscoelastic deformation. We do not allow effective viscosities less than 10^{19} Pa, and thus the minimum Maxwell time is about 10 yr. (2) The time step has to be less than the time required for propagation of elastic deformation half a grid space. This is proportional to the grid spacing divided by the elastic wave speed. A 2 km grid spacing and a wave speed of ~ 10 km s^{-1} yields a time step under a second.

To consider subduction on a time scale of millions of years using such a small time step would require inordinate computation times. To overcome this problem, we followed Cundall[36] and decreased the model elastic wave speed. Using this approach other groups have shown that setting the wave speed to be ~10^5 times the boundary velocity gives results that do not depend significantly on the time step and this speeds up calculations by more than a million times[60,61]. We used the same time step (~0.5 yr) both for the development of the subduction system over millions of years and for the 1,000 yr-long interseismic period (the assumed time between earthquakes that involve a complete loss of stress on the subduction interface) when the interface is locked.

As in previous subduction models[37], the initiation of subduction requires 'seeding' an area of weakness in the centre of the domain while the oceanic plate is pushed from the side. As f_2 and C_2 are both set to zero, the initial seed evolves into an area of high plastic strain that forms a weak subduction interface. As in earlier models of strain localization, the region of weakness is about three elements wide[53]. The interface shape and depth change with time according to the imposed boundary conditions.

Subduction is driven by a constant horizontal–velocity boundary condition on the vertical side (left side = 0 cm yr^{-1}, right side = 10 cm yr^{-1}) of the lithospheric plates (white arrows in Fig. 4). We set the boundary conditions to guarantee mass conservation and a free surface to accurately track the topography. The base of the domain is a Winkler foundation[60] and the sides are shear stress free.

Changes in the dip of the subducting plate may be caused by several factors, some of which have been considered in previous numerical studies[62–64]. In this work a gradual change of the subduction dip angle was produced by altering the motion of the upper plate relative to the deeper mantle[65]. This was done by changing the velocity boundary condition on the sides of the domain as illustrated in Fig. 4 (black arrows). To impose a decrease (increase) in the dip angle, we forced the asthenosphere to migrate in the same (opposite) horizontal direction of the downgoing plate. These boundary conditions were imposed over a depth range of 100–500 km. To reduce the computation time, we used higher values for the imposed relative velocity (10 cm yr^{-1}) than expected from observational constraints. We tested a number of relative velocities to validate that upper plate stress changes are not rate dependent (Supplementary Section 4).

To produce interseismic stresses after long-term subduction, we locked the interface at seismogenic depths (2–40 km) for 1,000 years by setting $f_2 = f_1$ and $C_2 = C_1$. We then simulated a megathrust earthquake by instantaneously changing f_2 and C_2 to zero, which changes the strength of the plate interface to zero. Modelled extensional aftershocks were flagged wherever extensional brittle yielding occurred after the imposition of zero strength on the interface. The ~10 MPa average shear stress drop on the interface after the reduction of friction is on the order of the mean stress drop estimated for the Tohoku earthquake[1]. Two hours after the simulated earthquake we changed f_2 and C_2 to their interseismic values.

To accurately follow the rapid stress changes during the co- and postseismic period, we set the compressional wave speed to its real value so the time step for stability was ~0.5 s. Our procedure is analogous to the somewhat more complex, adaptive time-step procedures used by other groups that simulate earthquakes over many seismic cycles[39], which include models using FLAC[38]. We verified our methodology with spatial and temporal resolutions tests, as described in the Supplementary Information.

Estimating slab dip changes based on the location of the volcanic arc. We define the dip angle as the arctangent of the ratio of the depth of the top of the slab beneath the volcanic arc (H) to the distance (L) from the arc to the trench. To estimate L for different locations of the arc, we measured the distance of the current and past arcs[43] to the trench at 37° N latitude. We assumed the trench has not moved relative to the island of Honshu.

H is taken to be the depth of the top of the Wadati–Benioff zone, found to be 100 km for the present day arc in Honshu[66]. A global compilation of the depth of the Wadati–Benioff zone for different subduction zones suggests that H varies from values ranging from 72 to 173 km with an average of 105 km. Thus, it is possible that the value of H in Honshu has changed with time. We used this variance to estimate the error bars for the dip angle of the subduction zone in the past. Error bars in the timing of the different dips are taken to be those of the suggested timing of the location of the arc[43].

Data availability

Source data for Fig. 2 are provided as a Source Data file. The location and timing of aftershocks for the Tohoku, Sumatra–Andaman and Java events can be found in the Iris catalogue (http://service.iris.edu/fdsnws/event/1/) or by contacting the corresponding authors of the aftershocks papers cited within this article.

Code availability

The numerical code we used for these model runs can be found at https://bitbucket.org/tan2/flac/src/default/.

References

51. Kanamori, H. & Kikuchi, M. The 1992 Nicaragua earthquake: a slow tsunami earthquake associated with subducted sediments. *Nature* **361**, 714–716 (1993).
52. Satake, K. & Tanioka, Y. Sources of tsunami and tsunamigenic earthquakes in subduction zones. *Pure Appl. Geophys.* **154**, 467–483 (1999).
53. Lavier, L. L., Buck, W. R. & Poliakov, A. N. B. Factors controlling normal fault offset in an ideal brittle layer. *J. Geophys. Res. Solid Earth* **105**, 23431–23442 (2000).
54. Poliakov, A. N. B., Podladchikov, Y. & Talbot, C. Initiation of salt diapirs with frictional overburdens: numerical experiments. *Tectonophysics* **228**, 199–210 (1993).
55. Lavier, L. L. & Buck, W. R. Half graben versus large-offset low-angle normal fault: importance of keeping cool during normal faulting. *J. Geophys. Res.* **107**, 2122 (2002).
56. Qin, R. & Buck, W. R. Why meter-wide dikes at oceanic spreading centers? *Earth Planet. Sci. Lett.* **265**, 466–474 (2008).
57. Hall, C. E., Gurnis, M., Sdrolias, M., Lavier, L. L. & Müller, R. D. Catastrophic initiation of subduction following forced convergence across fracture zones. *Earth Planet. Sci. Lett.* **212**, 15–30 (2003).
58. Karato & Wu Rheology of the upper mantle: a synthesis. *Science* **260**, 771–778 (1993).
59. Jaeger, J. C., Cook, N. G. W. & Zimmerman, R. *Fundamentals of Rock Mechanics* 4th edn (Wiley, 2007).
60. Poliakov, A. N. B. & Buck, W. R. Mechanics of stretching elastic-plastic-viscous layers: applications to slow-spreading mid-ocean ridges. *Geophys. Monogr. Ser.* **106**, 305–323 (1998).
61. Choi, E., Buck, W. R., Lavier, L. L. & Petersen, K. D. Using core complex geometry to constrain fault strength. *Geophys. Res. Lett.* **40**, 3863–3867 (2013).
62. Martinod, J. et al. How do subduction processes contribute to forearc Andean uplift? Insights from numerical models. *J. Geodyn.* **96**, 6–18 (2016).
63. Hassani, R., Jongmans, D. & Chéry, J. Study of plate deformation and stress in subduction processes using two-dimensional numerical models. *J. Geophys. Res. Solid Earth* **102**, 17951–17952 (1997).
64. Guillaume, B., Hertgen, S., Martinod, J. & Cerpa, N. G. Slab dip, surface tectonics: how and when do they change following an acceleration/slow down of the overriding plate? *Tectonophysics* **726**, 110–120 (2018).
65. Scholz, C. H. & Campos, J. On the mechanism of seismic decoupling and back arc spreading at subduction zones. *J. Geophys. Res. Solid Earth* **100**, 22103–22115 (1995).
66. Syracuse, E. M. & Abers, G. A. Global compilation of variations in slab depth beneath arc volcanoes and implications. *Geochem. Geophys. Geosyst.* **7**, Q05017 (2006).

Acknowledgements

We thank M. Steckler and H. Savage for their support and comments and for suggestions made by G. Coffey. We are appreciative of K. Key and his group for letting us use their computational resources. This project was supported by NSF EAR 17-14892. Lamont-Doherty Earth Observatory publication no. 8382.

Author contributions

B.O. wrote sections of the code applicable for this project, ran the models and analysed the results. W.R.B. planned and oversaw the study. B.O. wrote and W.R.B. edited the manuscript.

Competing interests

The authors declare no competing interests.

Additional information

Supplementary information is available for this paper at https://doi.org/10.1038/s41561-020-0553-x.

Correspondence and requests for materials should be addressed to B.O.

Peer review information Primary Handling Editors: James Super; Melissa Plail.

Reprints and permissions information is available at www.nature.com/reprints.